






Dependence of nonlinear coupling among turbulence, geodesic acoustic modes and tearing modes on magnetic island width in the HL-2A edge plasmas

J.Q. Xu¹, J.C. Li^{2,*}, X.D. Peng¹, Y.R. Qu³, Z. Lin⁴, M. Jiang¹, Z.H. Huang¹, N. Wu¹, W.C. Wang¹, G.Z. Hao¹, W. Chen¹, H.P. Qu¹, J.Q. Li¹, M. Xu¹ and the HL-2A Team¹

¹ Southwestern Institute of Physics, PO Box 432, Chengdu 610041, China

² Department of Earth and Space Sciences, Southern University of Science and Technology, Shenzhen, Guangdong 518055, China

³ School of Physics, Nankai University, Tianjin 300071, China

⁴ University of California, Irvine, CA 92697, United States of America

E-mail: jingchunli@pku.edu.cn and lijc@sustech.edu.cn

Received 30 May 2022, revised 14 September 2022

Accepted for publication 16 September 2022

Published 19 October 2022



CrossMark

Abstract

Statistical spectral features of the dependence of geodesic acoustic modes (GAMs) and their nonlinear couplings with ambient turbulence on the magnetic island (MI) width (W) in the edge region of HL-2A tokamak plasmas are analyzed. Experimental observations have indicated that the modulation influence as well as the strength of nonlinear interactions between GAMs and turbulence generally shows a gradual decay while the couplings between MIs and the latter are increased simultaneously as the MI becomes larger. The MIs mainly reduce the couplings between GAMs and potential fluctuations, whereas the changes in the nonlinear interactions between density fluctuations and MIs are more evident. Moreover, it is found that there exists a nonmonotonic relationship between the turbulence correlation length and island width, in which it exhibits a minimum around $W \sim 3.7$ cm, suggesting that the MI around such a scale would have a significant suppression effect on turbulent transport. These findings promote the understanding of the nonlinear interactions between MIs and turbulence in the edge of fusion plasmas.

Keywords: magnetic island, geodesic acoustic mode, turbulence, nonlinear coupling

(Some figures may appear in colour only in the online journal)

1. Introduction

Understanding the physics of multiscale interactions between macroscale magnetohydrodynamic (MHD) instabilities and microscale turbulence is a crucial topic in magnetically confined plasma research which has attracted much attention recently [1–3]. The MHD instabilities will lead to global perturbations as well as distortion of the equilibrium magnetic

flux surfaces and may trigger major disruption due to the rotation and locking of the magnetic island (MI) [4], among which the tearing mode (TM) [5–7] is a typical resistive MHD instability that is frequently observed in tokamak plasmas. The drift-wave microturbulence [8], driven by various kinds of gradients, is another obstacle to achieving high-performance fusion plasmas as it will result in anomalous heat and particle transports, thus causing the degradation of confinement [9]. Meanwhile, plenty of experimental and simulated evidence has

* Author to whom any correspondence should be addressed.

indicated that mesoscale zonal flows (ZFs) [10] will be excited in drift-wave turbulence through nonlinear three-wave interactions which can regulate ambient fluctuations and reduce the saturation amplitude of the microturbulence, including the low frequency branch zonal flows (LFZFs) [11] and the high frequency branch geodesic acoustic modes (GAMs) [12–14]. Hence, the detailed investigation of the characteristics of cross-scale nonlinear interactions among these fluctuations is a key aspect in unraveling underlying mechanisms in the physics of fusion plasma.

Multiscale interactions among different spatial scales have been widely studied in the past, both numerically and experimentally. On the theoretical side, the self-consistent model was developed for describing the multiscale interaction between drift wave modes and TM in cylindrical plasmas, showing that the regulation of turbulence by sheared poloidal flow and the modification of the turbulence profile by TM act synergistically, forming a feedback loop [15]. The turbulence driven magnetic island (TDMI) has also been discovered in fluid simulations, where it is shown the MI is formed due to a nonlinear beating of the fastest growing small scale modes even when the TM is marginally stable or unstable [16]. Gyrokinetic simulations have also demonstrated that the electromagnetic turbulence is able to seed the MI whose nonlinear evolution depends on the plasma beta and equilibrium pressure gradient [17]. On the experimental side, the behavior of low frequency flows and background turbulence nearby stationary MIs induced by static resonant magnetic perturbations has been presented in J-TEXT [18], in which it is discovered that the GAM is damped in most of the edge area with MIs and the sign of the radial electric field changes from negative to positive inside the islands. The latter phenomenon is also demonstrated in LHD stellarator which provides a possible explanation for the link between the position of the transport barrier and the location of the low order rational surface [19]. The first evidence of localized modulation of large-scale turbulent density fluctuations by the neoclassical tearing mode has been reported in DIII-D tokamak [20] and multiscale interaction between MIs and microturbulence has been demonstrated through simultaneous 2D measurements of the turbulence and the temperature and poloidal flow profiles in KSTAR tokamak [21]. Recent experimental results have also suggested the coupling and interplay between MHD and turbulence, including turbulence spreading into the MI [22], self-organized change in topology and turbulence in the island [23] and the flow damping by a stochastic magnetic field [24]. In addition, experiments on the HL-2A tokamak have indicated that both the perpendicular flow and the density fluctuation are modulated by TM near the island boundary [25] and provided the first evidence that the modulation of turbulence occurs only when the island width exceeds a certain threshold value [26]. However, theoretical and numerical results reported in the literature are sparse due to the limitations of the computing facilities. The multiscale interactions causing the appearance of MI in the quasi-steady turbulent state including ZFs and GAMs are firstly presented by two-fluid simulations [27]. The effect of the islands on profiles, flows, turbulence and

transport and the scaling of these effects with respect to island width have been performed by local gyrokinetic simulations, showing that there exists a threshold island width, below which the islands have little or no effect, while beyond this point the islands significantly perturb flows and increase turbulence and transport [28].

Although great efforts have been made, most of these experiments and simulations concentrate on interactions in the core plasmas where the turbulence is mainly driven by ion temperature gradient (ITG) modes [29] or collisionless trapped electron modes [30]; however, the situation is quite different at the edge due to the collisional nature where the resistive pressure gradient driven modes are suspected to play an important role [31]. More importantly, the dominant components of ZFs in the core and edge are usually different and are characterized by LFZFs in the former and by GAMs in the latter, respectively. From this perspective, the experimental understanding of the nonlinear couplings among MIs, GAMs and turbulence, or trying to find experimental signatures of TDMIs in the edge region, are of great importance in promoting the understanding of the physics of multiscale interactions, which is the primary goal of the present paper.

The structure of this paper is as follows. In section 2, the experimental setup and spectral analysis techniques are described. Section 3 gives the experimental analysis results for data obtained from the HL-2A edge plasmas as well as the global gyrokinetic simulations in the presence of static MIs. Finally, concluding remarks are drawn in section 4.

2. Experimental setup and spectral techniques

The experiments were performed in a series of ohmically heated deuterium plasmas in the HL-2A tokamak [32] with the parameters of major radius $R = 1.65$ m, plasma minor radius $a \approx 0.30$ – 0.32 m, plasma current $I_p \approx 130$ – 150 kA, toroidal magnetic field $B_T \approx 1.3$ T and central line-averaged density $\bar{n}_e \approx 0.8$ – $1.1 \times 10^{19} \text{ m}^{-3}$. The fluctuations have been measured in the plasma boundary region using a fast reciprocating Langmuir probe (LP) system located at the outer middle plane [33] which has been used in the investigations of the dynamics of sheared flows [34] and L–I–H transitions [35] previously, as shown by the sketch in figure 1. The data from LP are digitized at the sampling frequency $f_s = 1$ MHz with 12 bit accuracy and the perturbation of the array to plasma is negligibly small. The local physical quantities can be calculated with the triple-tip principle. For example, the pins numbered (1, 2) and (3, 4) are pairs of standard double probes used to sample the ion saturation current, $I_{s1(2)} = (V_{1(5)} - V_{2(6)})/R_{\text{sample}}$ with R_{sample} being the sampling resistance. Pins numbered (4, 7) are used for detecting floating potentials (ϕ_f), from which the radial electric field E_r can be deduced from the two radially separated pins as $E_r = (\phi_{f4} - \phi_{f7})/\Delta r$. The distances are $\Delta r = 2.5$ mm and $\Delta\theta = 7.0$ mm, respectively. The local electron temperature and density are thus calculated as $T_{e1} = [V_2 - (\phi_{f3} + \phi_{f4})/2]/\ln 2$ and $n_{e1} = 2I_{s1}/[eA_{\text{eff}}(kT_e/m_i)^{0.5}]$, where A_{eff} , k and m_i stand for the effective area of 10.0 mm^2 , the Boltzmann coefficient and the ion mass, respectively.

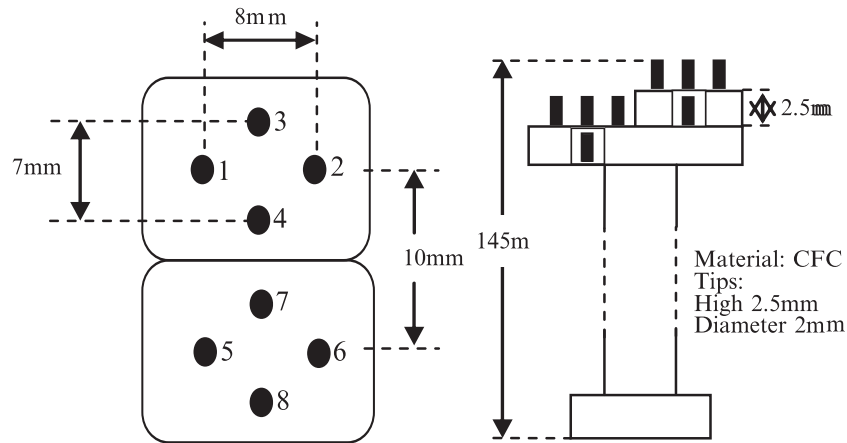


Figure 1. Configuration of the fast reciprocating probe array on HL-2A.

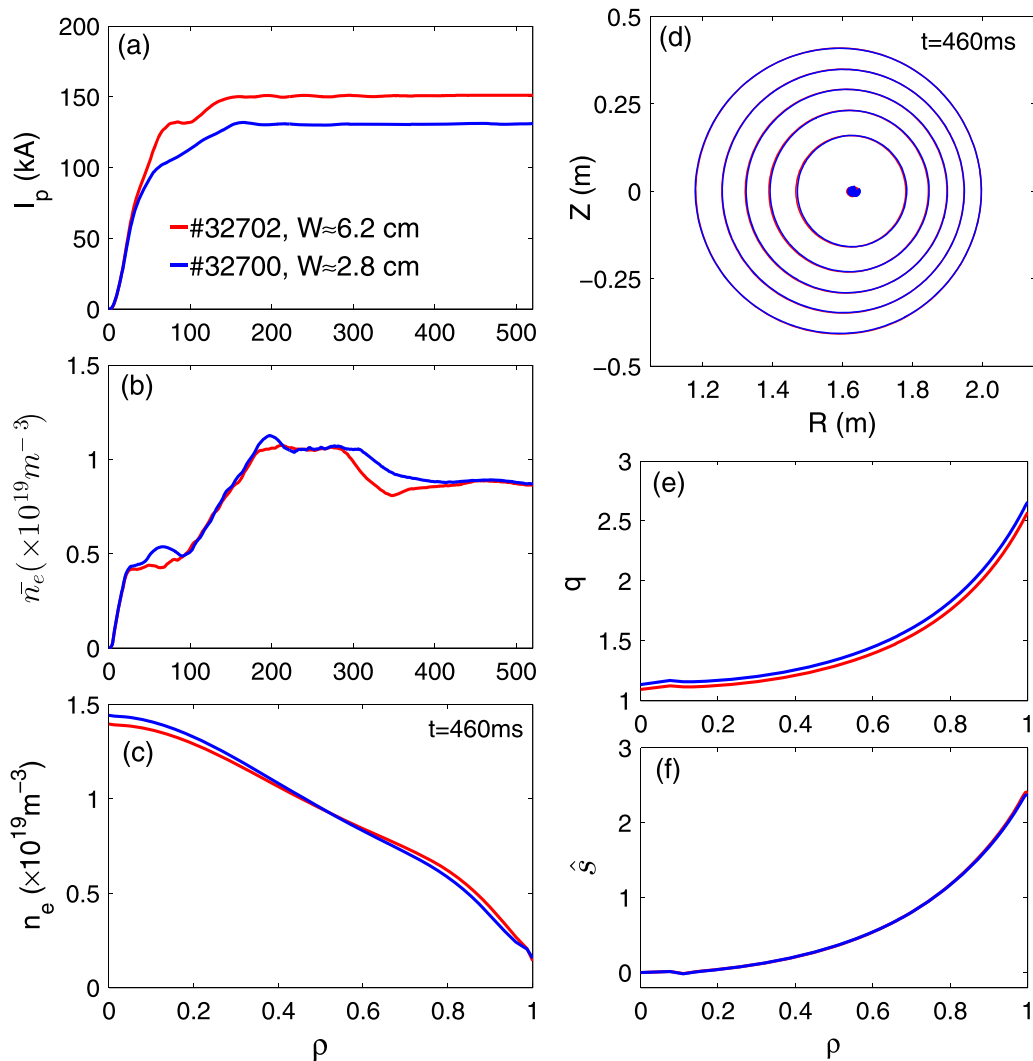


Figure 2. Typical discharge waveforms of (a) plasma current, (b) line-averaged density, (c) Electron density profile, (d) flux surface shape, (e) safety factor profile and (f) magnetic shear profile for MI widths of $W \approx 6.2$ cm (red) and $W \approx 2.8$ cm (blue).

In this paper, the analysis methods used to characterize the statistical spectral feature of turbulence and the nonlinear coupling among MIs, GAMs and turbulence are mainly the bispectrum and two-point correlation techniques. The bispectral

analysis technique [36] is a direct experimental confirmation for the nonlinear three-wave interactions among the fluctuating quantities. The squared bicoherence for fluctuating signals $x(t)$, $y(t)$ and $z(t)$ with their Fourier transforms $X(f)$, $Y(f)$ and

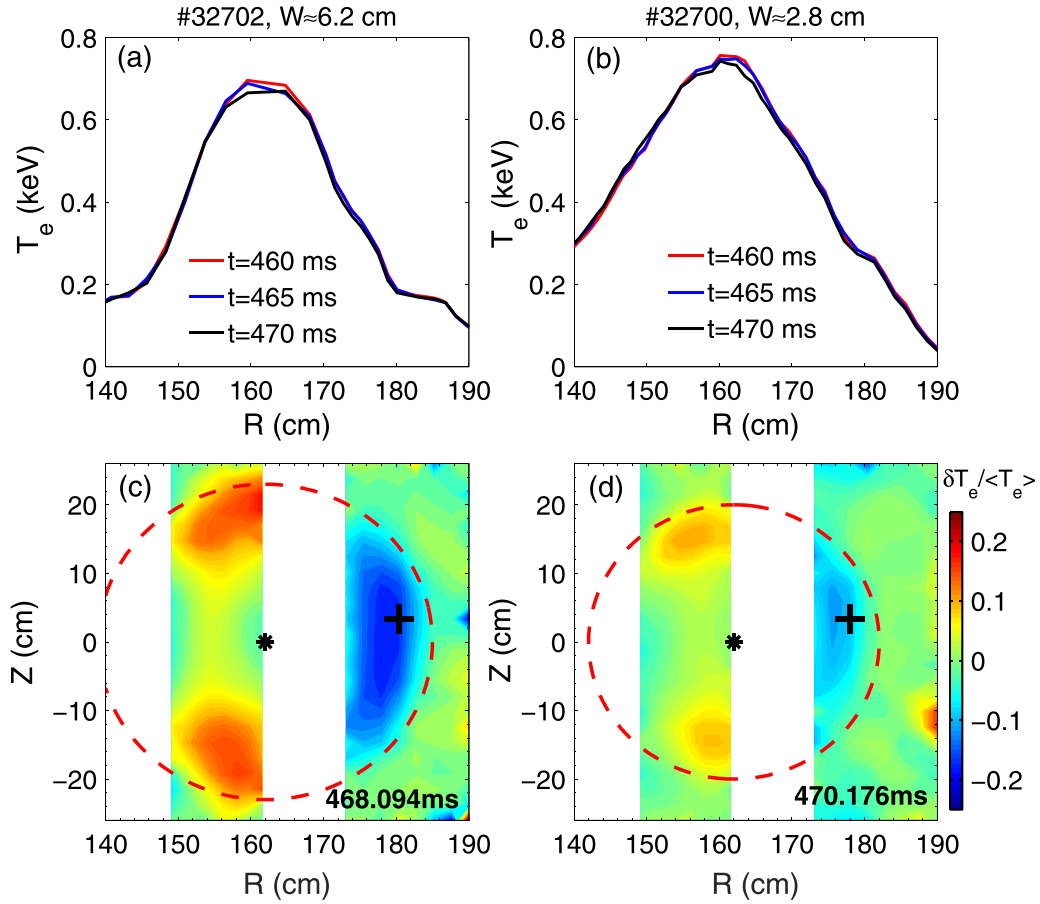


Figure 3. Electron temperature profiles and mode structure measured by ECE and ECEI. (a) and (b) are the profiles while (c) and (d) are the mode structure for MI widths of $W \approx 6.2$ cm and $W \approx 2.8$ cm, respectively.

$Z(f)$ is defined by

$$\hat{b}_{XYZ}^2(f_1, f_2) = \frac{|\hat{B}_{XYZ}(f_1, f_2)|^2}{\langle |X(f_1)Y(f_2)|^2 \rangle \langle |Z(f_3 = f_1 + f_2)|^2 \rangle} \quad (1)$$

where $\hat{B}_{XYZ}(f_1, f_2) = \langle X(f_1)Y(f_2)Z^*(f_3 = f_1 + f_2) \rangle$ is the bispectrum, which is called the auto-bispectrum when $X(f) = Y(f) = Z(f)$ and the cross-bispectrum in other cases. The summed squared bicoherence $\sum \hat{b}_{XYZ}^2(f_3)$ is defined as a sum of $\hat{b}_{XYZ}^2(f_1, f_2)$ for all f_1 and f_2 satisfying the frequency matching condition $f_3 = f_1 + f_2$ and normalized by the number $N(f_3)$ of Fourier components for each f_3 in the summations, i.e., $\sum \hat{b}_{XYZ}^2(f_3) = \sum_{f_3=f_1+f_2} \hat{b}_{XYZ}^2(f_1, f_2) / N(f_3)$, which provides a measure of the coherent three-wave coupling for all frequencies satisfying the resonance condition $f_3 = f_1 + f_2$. The fast Fourier transform bispectrum analysis is applied in the data processing with a typical data length larger than 100 ms in order to guarantee sufficient amount of ensemble average.

The two-point correlation technique [37] can provide a wealth of quantitative information about the structure of the turbulence and ZFs based on the assumption that fluctuations can be described as a superposition of wave packets each being characterized by a stochastic relationship between wavenumber $k(f)$ and frequency f . This technique gives a good estimate of the local statistical dispersion relation when changes in

amplitude and wavenumber of fluctuations are small over the distance of one wavelength. The values of the correlation length (L_c) are estimated as the inverse of the k spectrum broadening as

$$L_c = 1 / \int \bar{\sigma}_k^2 df, \quad \bar{\sigma}_k^2(f) = \frac{\int [k - \bar{k}(f)]^2 S(k, f) dk}{\int S(k, f) dk} \quad (2)$$

where $\bar{\sigma}_k^2(f)$ is the wavenumber spectrum width. The local wavenumber-frequency spectrum $S(k, f)$ is defined as $S(k, f) = \frac{1}{M} \sum_{j=1}^M I_{\Delta k}[k - k^j(f)] |S_1^j(f) + S_2^j(f)| / 2$, where $I_h(x)$ is the indicator function. S_1^j and S_2^j are power spectra measured at two positions with the separation of $\Delta x \leq \pi / k_{\max}$ and k_{\max} is the maximum wavenumber of fluctuations to be measured. $k^j(f) = \Delta \theta_{12}^j(f) / \Delta x$ is the local wavenumber, $\Delta \theta_{12}^j(f)$ is the phase shift between two points for each realization j , and M is the total realization number, respectively. The poloidal and radial correlation lengths are calculated by the two poloidally and radially separated probe pins measuring the floating potentials in this paper.

3. Experimental results

The typical discharge waveforms and magnetic configurations are shown in figure 2 for two different MI widths of

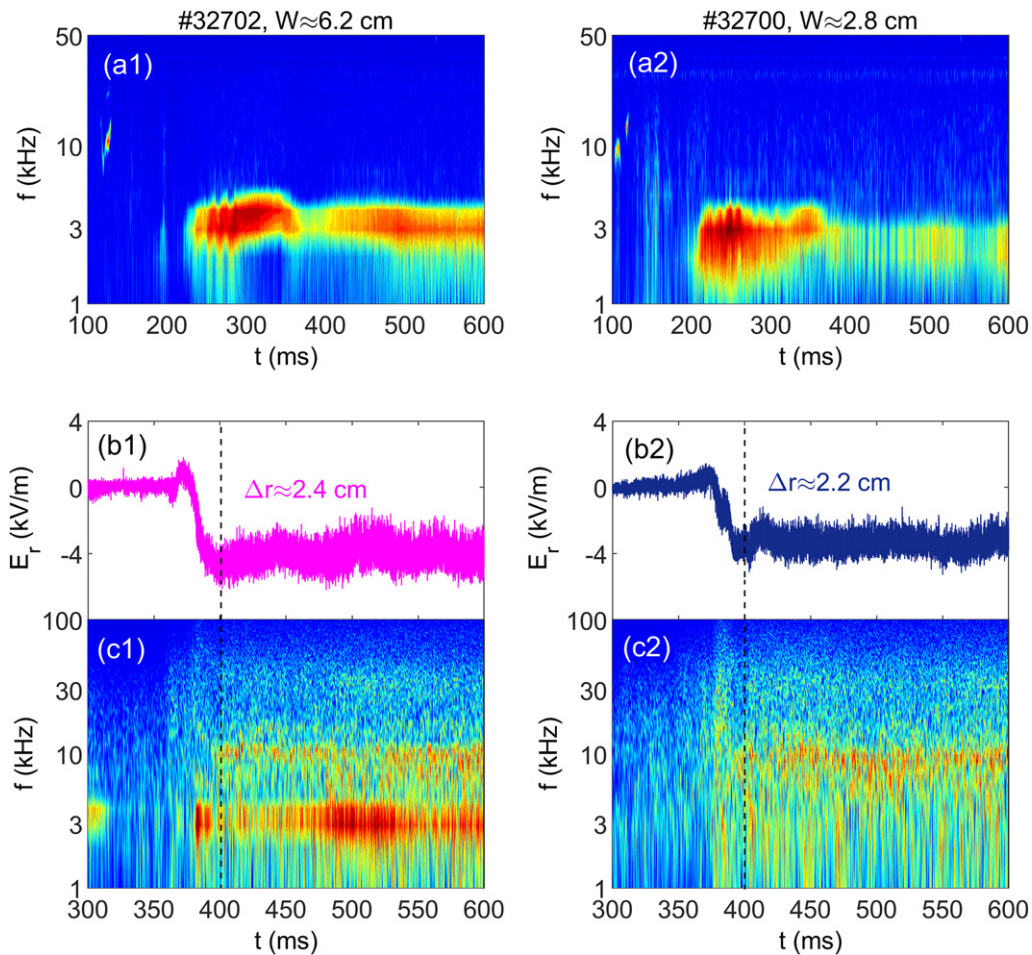


Figure 4. Spectrogram of SXR signal, time evolution of radial electric field and its spectrum for two values of MI widths. (a1)–(c1) Case for $W \approx 6.2$ cm; (a2)–(c2) case for $W \approx 2.8$ cm, respectively.

$W \approx 6.2$ cm and $W \approx 2.8$ cm. The flux surfaces and safety factor (q) profiles are calculated by the equilibrium and reconstruction fitting code while the density profiles are reconstructed from the hydrogen cyanide formic acid (HCOOH) laser interferometer [38] measurements through Abel inversion method. It is clearly shown in figures 2(c) and (d) that the electron density profiles and the magnetic flux surfaces have rather small difference for the two discharges, whereas the difference in q profiles are suggested to be resulted from the changes in the plasma current, i.e., the lower plasma current the higher safety factor. The island width depends on the linear stability of the TMs which is mainly controlled by varying the plasmas current hence the q profiles, as shown by figures 2(a) and (e). Analytical calculations have indicated that the values of TM stability indexes Δ' are positive at (2, 1) rational surfaces for both cases and gyrokinetic simulations employing GTC code [39–41] have shown that the TMs are unstable in both cases whose growth rates are around $\gamma = 0.052$ for shot 32702 and $\gamma = 0.043$ for shot 32700, respectively. The results have suggested that the TMs are unstable and the island width in shot 32702 is larger. Although it is impossible that a fixed island width being obtained even though the discharge parameters are the same, it is suggested that the change of island width in a series of similar discharges is relatively small,

which can be treated as the standard deviation of the island width during the steady state in a single shot. The errors of the island width are evaluated by typically ten ensembles for each shot with one sample data length of 20 ms. The background fluctuations modulated by MIs are observable on probes as the positions of the low order rational surfaces, for instance, $q = m/n = 2/1$ or $q = 3/2$ (with m and n being the poloidal and toroidal mode numbers, respectively) will suffer a gradual outward movement with the increasing of plasma current and the MI will become larger.

The corresponding electron temperature (T_e) profiles and mode structures measured by electron cyclotron emission (ECE) and the ECE imaging (ECEI) [42] systems are shown in figure 3. It is identified that the MIs are resulted from (m/n) = (2/1) classical TMs and the widths can be evaluated by either the flattened regions of the T_e profiles in figures 3(a) and (b) or the correlation lengths of the mode structures in figures 3(c) and (d). It should be noted that the ECEI or the ECE data is not accurate in determining the island widths in other shots especially for the cases of $W < 2$ cm. The signature of MI can be resolved by the spectrums of fluctuations on the probes using potential/radial electric field and density fluctuations in addition to magnetic perturbations if the MIs are large enough. The reason is that the MIs will

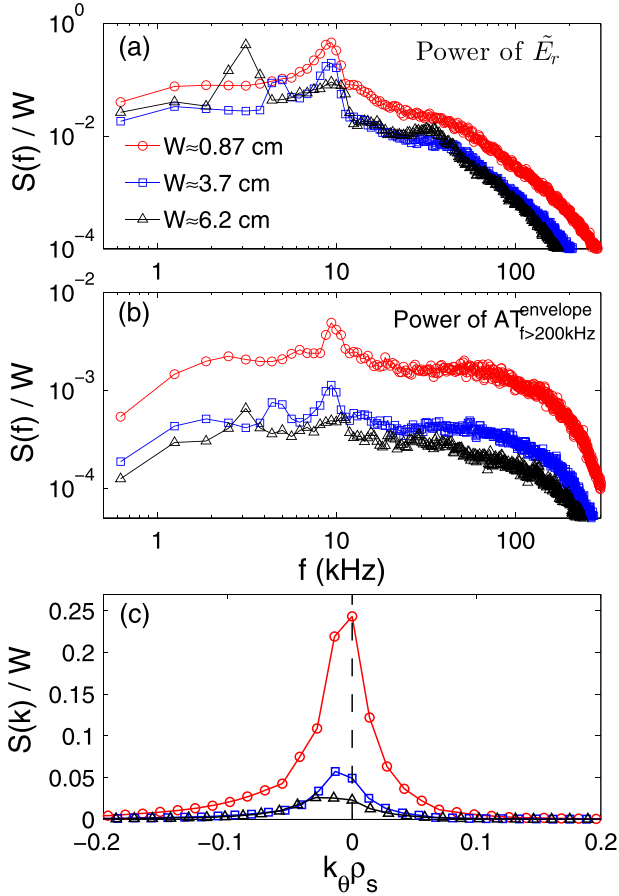


Figure 5. Power spectrums of (a) electric field fluctuation \tilde{E}_r , (b) envelope of density fluctuation \tilde{n}_e with $f > 200$ kHz and (c) normalized poloidal wavenumber for three different island widths.

modulate the background turbulence around them and once the probe position is close the island boundary these low frequency modes can be detected on both the spectrums of the fluctuations and envelopes of the high frequency bands. In the present study, the probe position is almost fixed but the island width is increased due to the change in the q profile when scanning the plasma current. The peaks at around $f \sim 3.2$ kHz in the spectrums of density and electric field fluctuations are identified to be resulted from the MIs, which have also been confirmed by other diagnostics such as Doppler backscattering [26]. The island widths of less than $W = 2$ cm can be estimated by calibrating them using the magnetic fluctuations and the soft-x ray (SXR) signals at a fixed position in the series of discharges. Although such a method would result in relatively large errors, the dependence of the spectral features of GAMs and turbulence as well as the nonlinear couplings can be well identified once the ambient fluctuations are modulated by the MIs and resolved by the probes.

Shown in figure 4 are the power spectrums of the SXR signals, the time trace of the radial electric fields (E_r) measured by the probe and their spectrums for two different island widths of $W \approx 6.2$ cm and $W \approx 2.8$ cm. The MIs with frequencies of about $f \sim 3.2$ kHz are observed in both cases on the SXR signals and the amplitude in the case of $W \approx 6.2$ cm is significantly larger than that of $W \approx 2.8$ cm, as can be

inferred from figures 4(a1) and (a2). In order to detect the GAMs and turbulence, the probes are inserted into the edge plasma whose radial positions with respect to the last closed flux surface during the steady state are around $\Delta r \approx 2.4$ cm and $\Delta r \approx 2.2$ cm, corresponding to a normalized radius of $\rho = r/a \approx 0.93$ and 0.94 , respectively, as illustrated in figures 4(b1) and (b2). The differences in probe positions in the series of discharges are relative small so as to eliminate the influence of positions on the GAM activities and turbulence and to make a quantitative comparison of the statistical features of the ZFs and turbulence. The noticeable coexistence of coherent modes at $f \sim 3.2$ kHz and $f \sim 9.4$ kHz during the steady state of probes are found for the case of $W \approx 6.2$ cm, whereas in the case of $W \approx 2.8$ cm only coherent fluctuation whose central frequency at about $f \sim 9.2$ kHz is observed. The mode at $f \sim 3.2$ kHz results from TM while the modes centered at $f \sim 9.4$ kHz and 9.2 kHz are identified to be GAMs [34, 43–45], whose frequencies are consistent with the theoretical prediction that $f_{\text{GAM}}^{\text{th}} \sim c_s \sqrt{2 + 1/q^2} / (2\pi R) = 9.3$ kHz calculated at $T_e \sim 90$ eV in both shots. Here, $c_s = \sqrt{T_e/m_i}$ is the ion sound speed. The island width in the latter situation is quite close to the threshold value where clear modulation and nonlinear coupling between TMs and turbulence can be well distinguished, as we will discuss in the following. Besides, it is discovered that the amplitude as well as the frequency spectrum broadening of GAMs are decreased in the former case, together with a reduction of high frequency background turbulence, suggesting that the GAMs, in addition to turbulence, will be suppressed in the presence of TMs, as can be concluded by the comparison between figures 4(c1) and (c2).

The modulation effect of MIs and GAMs on turbulence can be evaluated by the spectrum of the envelope of the high frequency turbulence, which is defined as the analytical signal employing Hilbert transform of a real signal $S_r(t)$ as $\hat{S}_r(t) = \frac{1}{\pi} \int_{-\infty}^{+\infty} \frac{S_r(\tau)}{t-\tau} d\tau$ which donates the modulus of the analytic signal. The power spectrum of \tilde{E}_r and the envelope of the high frequency component ($f > 200$ kHz) of density fluctuation \tilde{n}_e are shown in figures 5(a) and (b), while the normalized poloidal wavenumber spectrum is illustrated in figure 5(c), respectively. Here the frequency bands in figure 5(b) are selected corresponding to figure 6, in which it is shown that the change in bicoherence mainly occurs at $f > 200$ kHz. Similar to the summed bicoherence, both the amplitudes of \tilde{E}_r and the envelope of high frequency turbulence are reduced at GAM frequency whereas they are increased at the MI frequency as the island becomes larger, suggesting that the existence of MIs will suppress the GAMs, and their regulation effect on turbulence will be taken over if the MI is sufficiently strong, as can be inferred from figures 5(a) and (b). These relations still hold for the wavenumber spectrum, in which the modes with a wavenumber around $k_\theta \rho_s \sim 0$ donating the GAMs are weakened once the island width increases. The peaks at $k_\theta \rho_s \sim -0.015$ result from the MI fluctuations for the cases of $W \approx 3.7$ cm and $W \approx 6.2$ cm, where it is shown that the wavenumber spectrum will be modified due to the presence of MIs, as can be discovered from figure 5(c). Here the negative wavenumber donates that the mode rotates in the electron diamagnetic direction. The results also suggest that the MIs have

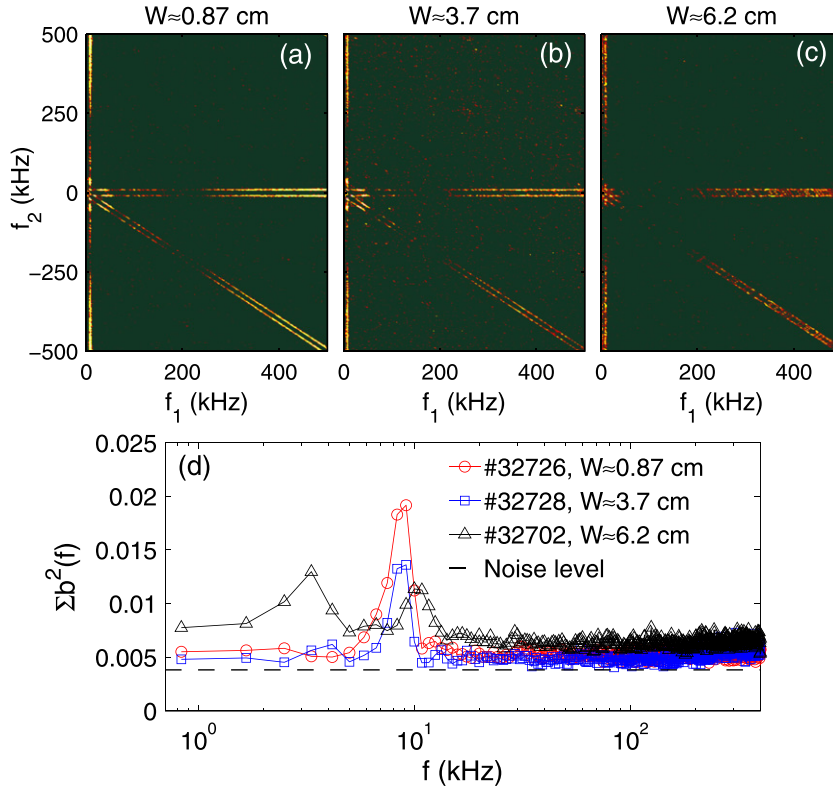


Figure 6. Contour plots of autocobherence of \vec{E}_r for the case of (a) $W \approx 0.87$ cm, (b) $W \approx 3.7$ cm and (c) $W \approx 6.2$ cm. (d) The corresponding summed squared bicoherence.

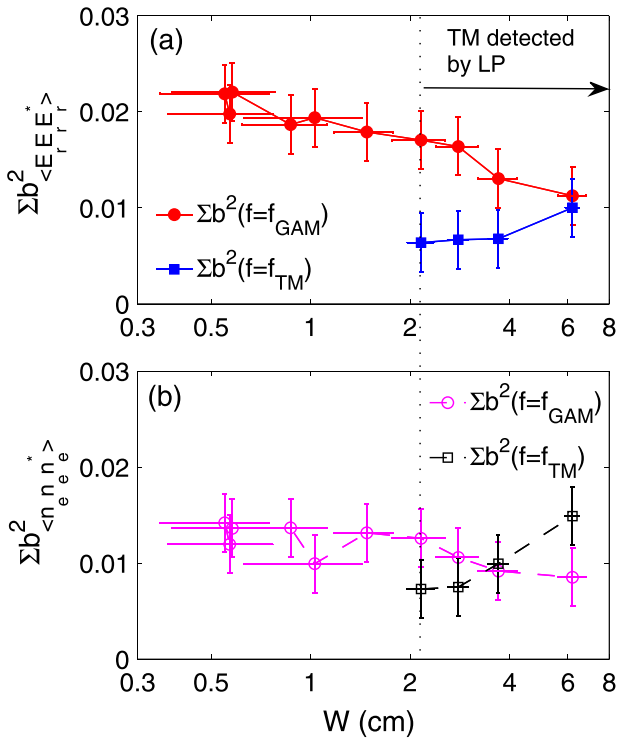


Figure 7. Dependence of summed squared bicoherence at the GAM and MI frequencies on island width using data of (a) electric field fluctuation \vec{E}_r and (b) density fluctuation \tilde{n}_e .

a strong impact on the background turbulence and they would decrease the coupling between GAMs and turbulence because

the role of GAM in regulating the turbulence is partially taken over by the MIs.

The nonlinear couplings between GAMs or MIs and the ambient turbulence can be verified through bispectrum analysis. The corresponding result for different island widths is shown in figure 6, in which three typical values of widths $W \approx 0.87$ cm, $W \approx 3.7$ cm and $W \approx 6.2$ cm are selected in order to give a distinct feature of the nonlinear interactions. Strong nonlinear coupling between GAM and high frequency turbulence is observed for the $W \approx 0.87$ cm whereas no signature is found at the MI frequency as the fluctuation of MI cannot be detected for small islands, as shown by the squared bicoherence in figure 6(a). The strength of the nonlinear coupling between GAM and turbulence is decreased while it is increased between MI and the latter as the island becomes larger, as indicated in figures 6(b) and (c) for $W \approx 3.7$ cm and $W \approx 6.2$ cm. It is also identified by the summed squared bicoherence in figure 6(d), where it is clearly shown that the nonlinear coupling between GAM and turbulence becomes weaker while the nonlinear interactions between MIs and turbulence becomes stronger simultaneously with the increasing of the island size.

The dependence of the nonlinear coupling among TMs, GAMs and turbulence on island width is shown in figure 7. The MI starts to be observable on probes when $W \approx 2.2$ cm. Below this value it is suggested that the changes in bicoherence is mainly resulted from variations of the probe positions and plasma displacements as the corresponding values are within the margin of statistical errors. Despite the above uncertainties, however, we can clearly find a decrease in the summed squared

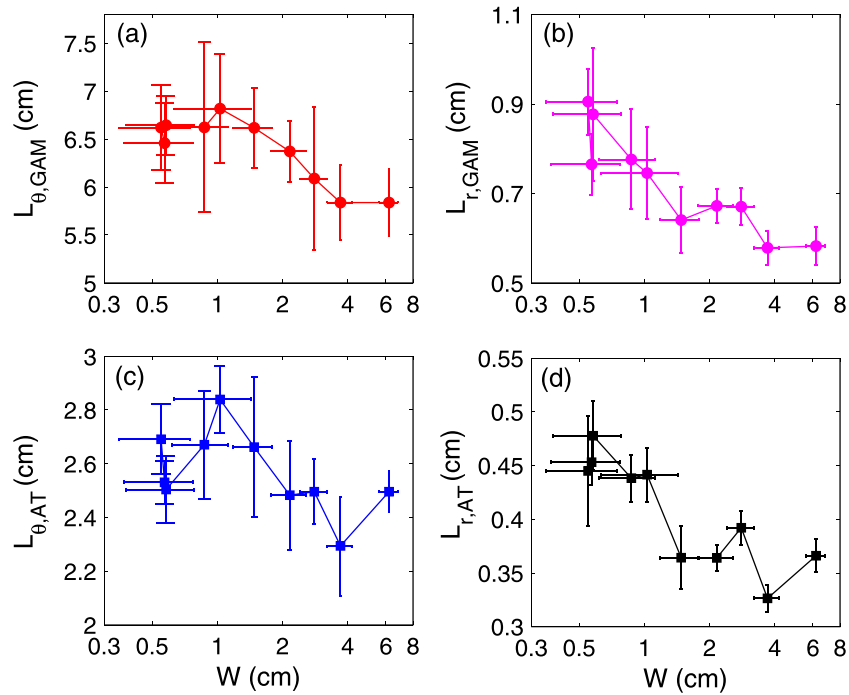


Figure 8. Poloidal and radial correlation lengths of GAMs and turbulence as a function of MI width. (a) and (b) Relationships for GAMs; (c) and (d) relationships for turbulence, respectively.

bicoherence at the GAM frequency and an increase at the MI frequency simultaneously with larger MI size for both electric field and density fluctuations. Besides, it is discovered that the dependence of the nonlinear coupling between GAM and turbulence is more obvious in electric field fluctuations, while it is more prominent between MI and turbulence in density fluctuations, implying that GAM mainly modulates the potential fluctuations whereas the MI has stronger regulation effect on density fluctuations, respectively.

Characterizing the effect of MI on turbulence is also important in understanding the physics of multiscale interactions and edge turbulent transport in the presence of TMs. While the long-range correlation is donated by the poloidal correlation length of GAM, the transport is mainly determined by the radial correlation length of turbulence. The corresponding poloidal and radial correlation lengths of GAMs are shown in figures 8(a) and (b), while those of turbulence are shown in figures 8(c) and (d), respectively. The frequency bands are selected as $f = 7\text{--}12$ kHz for GAMs and $f \geq 20$ kHz for turbulence, respectively. Generally we have noted that the data are only valid for $W \geq 0.87$ cm mainly due to the fact that the effect of MI cannot be effectively examined by the probes. Both the poloidal and radial correlation lengths of GAM $L_{\theta,GAM}$ and $L_{r,GAM}$ show a gradual reduction when W ranges from 0.87 cm to 3.7 cm. It seems that a larger island would not further change the $L_{\theta,GAM}$ or $L_{r,GAM}$, as can be found in figures 8(a) and (b). However, the correlation lengths of turbulence $L_{\theta,turb}$ and $L_{r,turb}$ have nonmonotonic relationships with W , which show minimum at $W \approx 3.7$ cm, implying that the MIs around this width have relatively strong suppression effect on turbulent transport. The underlying physics is still unclear at

this moment and the precise value of the island width having strongest suppression effect on ambient turbulence is also unavailable due to the lack of experimental data. Nevertheless, it is recommended that such relationship is reasonable which might be explained as follows: the MIs due to TMs suppress drift-wave instability by violating the ballooning structures of the micro-instabilities such as ITG and TEM and the spectrum of turbulence is broadened to produce the coherent vortex flows due to the modification of the parallel gradient by MIs [46]. This effect is only valid for small- and medium-sized MIs as an extremely large island may strongly change the magnetic topology and hence the turbulence nature. The measurements of parallel gradient in the presence of MIs and self-consistent gyrokinetic simulations based on the experimental data will be carried out in the future.

4. Concluding remarks

In this work, the dependence of nonlinear couplings among GAMs, TMs and turbulence on MI width in the edge plasma of HL-2A is presented. It is shown that the nonlinear coupling between GAMs and turbulence becomes weaker with increasing island width, while it becomes stronger between MIs and turbulence, indicating that the MIs will suppress the GAMs as well as their regulation effects on turbulence. The dependence of nonlinear coupling between GAM and turbulence is more obvious in electric field fluctuations, while it is more distinct between MI and turbulence in density fluctuations, implying that GAM and MIs mainly modulate the potential and density fluctuations, respectively. The poloidal and radial correlation lengths of GAMs generally show a decrease for small and

medium-sized islands whereas nonmonotonic relationships are discovered between the lengths of turbulence and island width which have a minimum of around $W \sim 3.7$ cm, suggesting a significant suppression effect on turbulent transport around such island size. Quantitative comparisons between experiments and self-consistent simulations of turbulence in the presence of rotating MIs will be carried out in the future.

Acknowledgments

This work was partly supported by National MCF energy R & D Program of China (Grant No. 2022YFE03060000), National Key R & D Program of China (Grant Nos. 2019YFE03020000, 2018YFE0303102 and 2017YFE0301200), National Natural Science Foundation of China (Grant Nos. 11947238, 11905109, 12075079, 12125502 and 11875019) and Sichuan Science and Technology Program (Grant No. 2021JDJQ0029). We also acknowledge the Center for Computational Science and Engineering of Southern University of Science and Technology for providing computational resources.

ORCID iDs

J.Q. Xu  <https://orcid.org/0000-0003-4834-3005>
 J.C. Li  <https://orcid.org/0000-0001-9918-8880>
 N. Wu  <https://orcid.org/0000-0001-7949-5330>
 G.Z. Hao  <https://orcid.org/0000-0003-2310-6134>
 W. Chen  <https://orcid.org/0000-0002-9382-6295>

References

- [1] Ida K. 2020 *Plasma Phys. Control. Fusion* **62** 014008
- [2] Ishizawa A., Kishimoto Y. and Nakamura Y. 2019 *Plasma Phys. Control. Fusion* **61** 054006
- [3] Choi M.J. 2021 *Rev. Mod. Plasma Phys.* **5** 9
- [4] Waelbroeck F.L. 2009 *Nucl. Fusion* **49** 104025
- [5] Furth H.P., Killeen J. and Rosenbluth M.N. 1963 *Phys. Fluids* **6** 459
- [6] Wesson J.A. 1978 *Nucl. Fusion* **18** 87
- [7] La Haye R.J. 2006 *Phys. Plasmas* **13** 055501
- [8] Tang W.M. 1978 *Nucl. Fusion* **18** 1089
- [9] Horton W. 1999 *Rev. Mod. Phys.* **71** 735
- [10] Diamond P.H., Itoh S.-I., Itoh K. and Hahm T.S. 2005 *Plasma Phys. Control. Fusion* **47** R35
- [11] Fujisawa A. et al 2004 *Phys. Rev. Lett.* **93** 165002
- [12] Winsor N., Johnson J.L. and Dawson J.M. 1968 *Phys. Fluids* **11** 2448
- [13] Shats M.G. and Solomon W.M. 2002 *Phys. Rev. Lett.* **88** 045001
- [14] Conway G.D., Smolyakov A.I. and Ido T. 2022 *Nucl. Fusion* **62** 013001
- [15] McDevitt C.J. and Diamond P.H. 2006 *Phys. Plasmas* **13** 032302
- [16] Muraglia M. et al 2011 *Phys. Rev. Lett.* **107** 095003
- [17] Hornsby W.A., Migliano P., Buchholz R., Grosshauser S., Weikl A., Zarzoso D., Casson F.J., Poli E. and Peeters A.G. 2016 *Plasma Phys. Control. Fusion* **58** 014028
- [18] Zhao K.J. et al 2015 *Nucl. Fusion* **55** 073022
- [19] Ida K. et al 2001 *Phys. Rev. Lett.* **88** 015002
- [20] Bardóczy L. et al 2016 *Phys. Rev. Lett.* **116** 215001
- [21] Choi M.J. et al 2021 *Nat. Commun.* **12** 375
- [22] Ida K. et al 2018 *Phys. Rev. Lett.* **120** 245001
- [23] Ida K. et al 2015 *Sci. Rep.* **5** 16165
- [24] Ida K. et al 2015 *Nat. Commun.* **6** 5816
- [25] Jiang M. et al 2018 *Nucl. Fusion* **58** 026002
- [26] Jiang M. et al 2019 *Nucl. Fusion* **59** 066019
- [27] Ishizawa A. and Nakajima N. 2007 *Phys. Plasmas* **14** 040702
- [28] Navarro A.B., Bardóczy L., Carter T.A., Jenko F. and Rhodes T.L. 2017 *Plasma Phys. Control. Fusion* **59** 034004
- [29] Romanelli F. 1989 *Phys. Fluids B* **1** 1018
- [30] Xiao Y. and Lin Z. 2009 *Phys. Rev. Lett.* **103** 085004
- [31] Bourdelle C., Garbet X., Singh R. and Schmitz L. 2012 *Plasma Phys. Control. Fusion* **54** 115003
- [32] Xu M. et al 2019 *Nucl. Fusion* **59** 112017
- [33] Yan L.W., Hong W.Y., Qian J., Luo C.W. and Pan L. 2005 *Rev. Sci. Instrum.* **76** 093506
- [34] Zhao K.J. et al 2006 *Phys. Rev. Lett.* **96** 255004
- [35] Cheng J. et al 2013 *Phys. Rev. Lett.* **110** 265002
- [36] Kim Y.C. and Powers E.J. 1979 *IEEE Trans. Plasma Sci.* **7** 120
- [37] Beall J.M., Kim Y.C. and Powers E.J. 1982 *J. Appl. Phys.* **53** 3933
- [38] Li Y.G. et al 2017 *Rev. Sci. Instrum.* **88** 083508
- [39] Lin Z., Hahm T.S., Lee W.W., Tang W.M. and White R.B. 1998 *Science* **281** 1835
- [40] Li J.C., Xiao C.J., Lin Z. and Wang K.J. 2017 *Phys. Plasmas* **24** 082508
- [41] Li J.C., Lin Z., Dong J.Q., Xie H.S. and Liu S.F. 2021 *Plasma Phys. Control. Fusion* **63** 125005
- [42] Jiang M. et al 2013 *Rev. Sci. Instrum.* **84** 113501
- [43] Cheng J. et al 2009 *Nucl. Fusion* **49** 085030
- [44] Lan T. et al 2008 *Plasma Phys. Control. Fusion* **50** 045002
- [45] Lan T. et al 2008 *Phys. Plasmas* **15** 056105
- [46] Ishizawa A. and Nakajima N. 2009 *Nucl. Fusion* **49** 055015